A&A 597, A118 (2017)
DOI: 10.1051/0004-6361/201526777


Astronomy & Astrophysics

# The Bok globule BHR 160: structure and star formation[⋆,⋆⋆]

L. K. Haikala[1] and B. Reipurth[2]

[1] Universidad de Atacama, Copayapu 485, Copiapo, Chile
e-mail: lauri.haikala@uda.cl
[2] Institute for Astronomy, University of Hawaii at Manoa, 640 N. Aohoku Place, Hilo, HI 96720, USA
e-mail: reipurth@ifa.hawaii.edu

Received 18 June 2015 / Accepted 31 August 2016

**ABSTRACT**

*Context.* BHR 160 is a virtually unstudied cometary globule within the Sco OB4 association in Scorpius at a distance of 1600 pc. It is part of a system of cometary clouds which face the luminous O star HD 155806. BHR 160 is special because it has an intense bright rim.
*Aims.* We attempt to derive physical parameters for BHR 160 and to understand its structure and the origin of its peculiar bright rim.
*Methods.* BHR 160 was mapped in the $^{12}$CO, $^{13}$CO and C$^{18}$O (2−1) and (1−0) and CS (3−2) and (2−1) lines. These data, augmented with stellar photometry derived from the ESO VVV survey, were used to derive the mass and distribution of molecular material in BHR 160 and its surroundings. Archival mid-infrared data from the WISE satellite was used to find IR excess stars in the globule and its neighbourhood.
*Results.* An elongated 1′ by 0.′6 core lies adjacent to the globule bright rim. $^{12}$CO emission covers the whole globule, but the $^{13}$CO, C$^{18}$O and CS emission is more concentrated to the core. The $^{12}$CO line profiles indicate the presence of outflowing material near the core, but the spatial resolution of the mm data is not sufficient for a detailed spatial analysis. The BHR 160 mass estimated from the C$^{18}$O mapping is $100 \pm 50\,M_{\odot}$ $(d/1.6\,\mathrm{kpc})^2$ where $d$ is the distance to the globule. Approximately 70% of the mass lies in the dense core. The total mass of molecular gas in the direction of BHR 160 is $210 \pm 80\,(d/1.6\,\mathrm{kpc})^2\,M_{\odot}$ when estimated from the more extended VVV near-infrared photometry. We argue that the bright rim of BHR 160 is produced by a close-by early B-type star, HD 319648, that was likely recently born in the globule. This star is likely to have triggered the formation of a source, IRS 1, that is embedded within the core of the globule and detected only in *K*s and by WISE and IRAS.

**Key words.** stars: formation – stars: pre-main sequence – ISM: individual objects: BHR 160 – dust, extinction

## 1. Introduction

Bok globules are small compact clouds with typical dimensions of approximately 0.15 to 0.8 pc (Bok 1977; Reipurth 2008). Many of these are cloud cores which have been exposed from the interior of large molecular clouds when the more tenuous material has been swept away by the formation of nearby OB stars (Reipurth 1983). Cometary globules are a subset of Bok globules in a transition phase, still showing the windswept appearance of their formation. The compression that the globules suffer as they are being excavated, in many cases leads to the formation of stars, so cometary globules are frequently containing young stars (for example Haikala & Reipurth 2010; Haikala et al. 2010).

In a survey for globules in the Galactic plane, we have come across a remarkable yet virtually unexplored cometary globule. It is listed as object 353.3+2.4 in the Hartley et al. (1986) list of southern dark clouds. Bourke et al. (1995a,b) surveyed the optical appearance of the opaque Hartley et al. (1986) clouds smaller than 10′ in diameter and searched for ammonia (1, 1) emission in this selection. Globule 353.3+2.4 is object 160 in the Bourke et al. (1995a) list and will be identified as BHR 160 in the following.

The globule is clearly cometary, but the striking aspect of it is its bright rim (Fig. 1). The brightest part of this rim has a width of ∼2′ (0.9 pc) with fainter extensions on both sides. We have obtained a poor, noisy red spectrum at the ESO 3.6 m telescope of the bright rim which shows a strong H$\alpha$ line and much weaker lines of [SII] $\lambda$ 6717/6731 lines, as expected in photoionized gas. None of the other cometary clouds in the region show similar bright rims, which leads to the suspicion that a bright star ∼30″ away from the midpoint of the bright rim is the source of UV radiation. This star is HD 319648, an early B star.

The general region of BHR 160 contains a number of cometary globules and cometary-shaped clouds, which all face towards another, more distant, bright star, HD 155806 (=HR 6397 = V1075 Sco), see Fig. 2. This is an O7.5Ve star (Walborn 1973), and the hottest known Galactic Oe star (Fullerton et al. 2011). HD 155806 is the most luminous star in the little-studied Sco OB4 association (Thé 1961; Roslund 1966). Within a radius of one degree around HD 155806, Thé (1961) found 40 OB stars and 85 A-type stars, for which he adopted a distance of ∼1400 pc. In a follow-up study, Roslund (1966) found that the Sco OB4 association extends towards the south, with its main concentration in the young H II region NGC 6334. Persi & Tapia (2008) have determined the distance to NGC 6334 to be 1.61 ± 0.08 kpc. In the following we adopt a distance of 1.6 kpc for BHR 160.

In this paper, we present detailed millimetre-wavelength multi-transition observations of the virtually unstudied globule

⋆ Based on observations made with ESO Telescopes at the La Silla or Paranal Observatories.
⋆⋆ Reduced molecular line spectra (The SEST spectra as FITS files) are only available at the CDS via anonymous ftp to cdsarc.u-strasbg.fr (130.79.128.5) or via http://cdsarc.u-strasbg.fr/viz-bin/qcat?J/A+A/597/A118

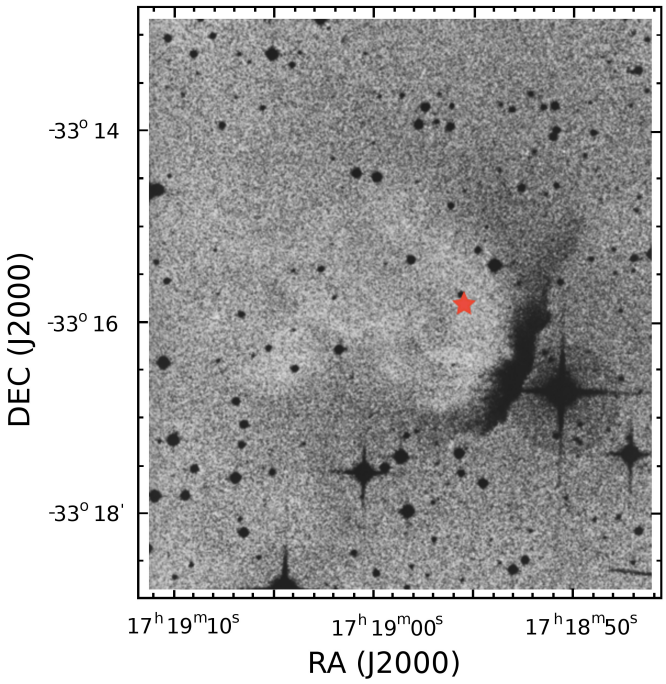


**Fig. 1.** Close-up of the BHR 160 globule from an ESO-R sky survey plate. The bright rim is striking in appearance. The bright star in front of the bright rim is the early B-type star HD 319648. The red asterisk marks the location of the embedded source IRS 1, see Fig. 4 and the text for details. The region between IRS 1 and the bright rim is here called "the core".


**Fig. 2.** Northern part of the Sco OB4 association includes the luminous O7.5V star HD 155806, towards which BHR 160 and other cometary-shaped clouds point. The area of Fig. 3, which includes BHR 160, is indicated by a rectangle. Image courtesy S. Guisard/ESO.

BHR 160, and we use the data to determine the mass and structure of the globule. The observations are augmented with archival near- and mid-infrared data which reveal that star formation is ongoing within the globule.

## 2. Observations and data reduction

The single BHR 160 ammonia (1, 1) spectrum in Bourke et al. (1995b) was a non-detection. This is probably explained by the 1.′4 HPBW of the Parkes telescope used in the survey. The beam covers practically the whole globule and a dense, small-size core is highly beam diluted. Spectral line observations with better spatial resolution and molecular species and transitions tracing also the more diffuse material in BHR 160 are called for. The CO molecule and its isotopologues trace gas column density, and especially the $^{12}$CO molecule is excited already at moderate densities. As the abundance of $^{13}$CO and C$^{18}$O is only a fraction of that of $^{12}$CO, their optical depths and consequently – because of less radiative trapping – their effective critical densities are higher. The CS molecule is a good tracer for high-density gas. This makes the CO (and isotopologues) (2−1) and (1−0) and the CS (3–2) and (2−1) transitions convenient tools when studying the basic properties of a moderately dense globule core and its less dense envelope.

The molecular line observations were obtained in September and October 1999 with the Swedish-ESO-Submillimetre-Telescope (SEST), at the La Silla observatory, Chile. The SEST 3 and 2 mm (SESIS) and 3 and 1 mm (IRAM) dual SiS SSB receivers were used. The IRAM receiver was used except when observing the CS lines, for which the SESIS receiver was used. The SEST high-resolution 2000 channel acousto-optical spectrometer (bandwidth 86 MHz, channel width 43 kHz) was split into two to measure two receivers simultaneously. At the observed wavelengths, 3 mm, 2 mm and 1 mm, the 43 kHz channel width corresponds to ∼0.12 km s$^{-1}$, ∼0.08 km s$^{-1}$ and ∼0.06 km s$^{-1}$, respectively.

**Table 1.** Observed lines and telescope parameters.

| Line | $\nu$ (GHz) | *HPBW* ($''$) | $\eta_{\rm mb}$ |
|---|---|---|---|
| CS (2−1) | 97.271 | 54 | 0.70 |
| CO (1−0) | 115.271 | 47 | 0.70 |
| CS (3–2) | 145.904 | 34 | 0.66 |
| CO (2−1) | 230.538 | 24 | 0.50 |

An approximately 2.′5 by 2.′5 area was observed with 20$''$ spacing and a tilt of 60°. The map was centred at 17$^{\rm h}$18$^{\rm m}$53.$^{\rm s}$1, −33°16′25$''$ (J2000). The CO (2−1) and (1−0) and the CS (3–2) and (2−1) transitions were observed simultaneously. Frequency switching observing mode was used. The switch was 5 MHz for the 1 mm and 15 MHz for 2 and 3 mm observations. A second-order baseline was subtracted from the spectra after folding. Calibration was achieved by the chopper wheel method. All the line temperatures in this paper, unless specially noted, are in the units of $T_{\rm A}^*$, that is corrected to outside of the atmosphere but not for beam coupling. Typical values for the effective SSB system temperatures outside the atmosphere were around 200 K except for the $^{12}$CO (1−0) line for which it was 350 K. The RMS of the spectra for one minute integration after folding was around 0.1 K except for CO (1−0) (0.15 K). Pointing accuracy is estimated to be better than 5$''$.

The observed molecular transitions, their frequencies, SEST half power beam width, HPBW, and the telescope main beam efficiency, $\eta_{\rm mb}$, at these frequencies are given in Table 1. For the

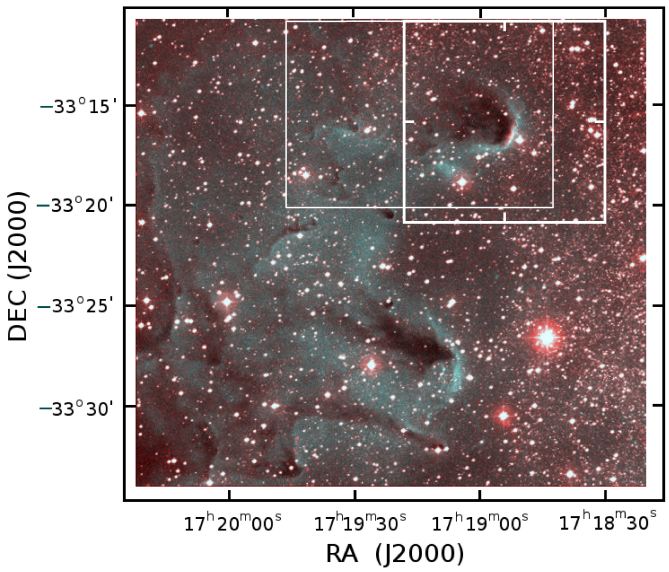


**Fig. 3.** AAO/UKST survey image of BHR 160 combining an H$\alpha$ image (blue) and a short red broadband image (red). BHR 160 is located in the upper right corner of the image, and the larger cloud to the south of NHR 160 is known as BHR 159. The rectangles indicate the location of Figs. 4 and 5.

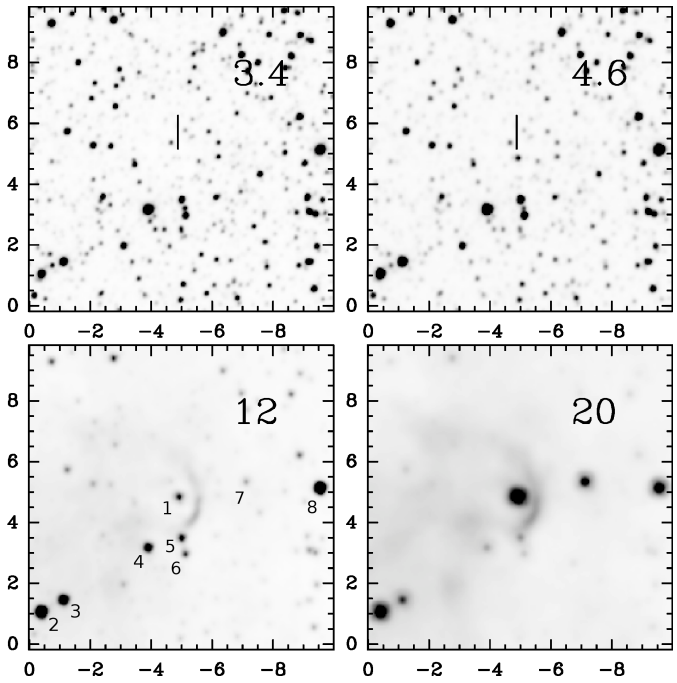


**Fig. 4.** WISE images at 3.4, 4.6, 12 and 20 $\mu$m. The location of BHR 160 IRS1 is indicated with a line in the two *upper panels* and with 1 in the *lower left panel*. Besides BHR 160 IRS1 seven further stellar sources emitting strongly at 12 $\mu$m are marked in the *latter panel*. The unit of the axes is arcminutes.

CO observations only the $^{12}$CO is listed. At a distance of 1.6 kpc the SEST HPBW at 230 GHz corresponds to 0.19 pc.

## 3. Results

### 3.1. Optical and infrared archival data

Survey data of the BHR 160 region can be found in the AAO/UKST H$\alpha$ survey (Parker et al. 2005), ESO VISTA variables in the Vía Láctea (VVV, Saito et al. 2012) survey, Wide-Field Infrared Survey Explorer (WISE, Wright et al. 2010) and IRAS public data bases. These data were used to evaluate the distribution of interstellar matter and properties of individual stellar sources in the region.

The colour coded image from the AAO/UKST H$\alpha$ survey (H$\alpha$ plus [NII] coded in blue) and short-exposure red-band (5900−6900 Å) image (in red) shown in Fig. 3 reveals that BHR 160 is in fact a part of a receding wall of an (extinct) HII region. One large cometary-shaped object (BHR 159) and several smaller globules lie to the south-east. The western edge of BHR 160 emits strongly in H$\alpha$ but the UKIDSS *Y* and *Z* images indicate that a part of the surface brightness is also reflected light. The source of the excitation is possibly the nearby B star HD 319648 located very close to the globule.

WISE imaged BHR 160 at 3.4, 4.6, 12 and 20 $\mu$m (Fig. 4). Only stars are visible in the direction of the globule at the shortest wavelengths 3.4 and 4.6 $\mu$m. A star in the centre of the globule (WISE J171855.54-331554.3), which is faint at 3.4 $\mu$m ($10\overset{m}{.}97$), becomes brighter at 4.6 $\mu$m and continues brightening at 12 and 20 $\mu$m. This WISE source will be referred to as BHR 160 IRS1 in the following. Besides BHR 160 IRS1 seven further stellar sources emitting strongly at 12 $\mu$m are marked in the figure. The globule bright rim is visible at the two longest wavelengths. Besides the bright rim, fainter surface brightness is also visible along the body of the globule. An IRAS point source IRAS 17156-3312 lies 15″ west of the WISE source. It has a good quality detection at 60 and 100 $\mu$m bands, 15.3 and 71.8 Jy, respectively. In the HIRES processed (Auman et al. 1990) IRAS images, the 60 $\mu$m emission maximum coincides with the WISE source, but the 100 $\mu$m emission maximum is shifted towards the bright rim. The spatial resolution of the IRAS 100 $\mu$m observations, even when HIRES-processed, is not sufficient to resolve the small scale structure in the globule. Therefore it is likely that part of the observed 100 $\mu$m emission comes from heated dust associated with the globule.

In the H$\alpha$ and the short-exposure red images (Fig. 3), optical extinction is high in an arc to the east of (behind) the bright rim, and a less extincted area continues to NE. This is in agreement with the ESO VISTA VVV survey *YZJHK* false colour image shown in Fig. 5. BHR 160 IRS 1 is not situated inside the dense elongated core but at its edge on the opposite side of the bright rim. A faint, slightly extended non-stellar red object detected only in the *Ks* band coincides with BHR 160 IRS1. The region of high extinction between the bright rim and BHR 160 IRS1 will be called "the core" in the following. No stars can be seen in the very centre of the core in Fig. 5.

### 3.2. Molecular line observations

Three velocity components are seen in the $^{12}$CO spectrum (Fig. 6) observed in the direction of BHR 160. The components will be referred to as C1, C2 and C3 as marked in the figure. Two negative line components are seen in this spectrum. The negative line component at ∼−10 km s$^{-1}$ is produced in the frequency switching technique by component C3. The negative signal at ∼−1 km s$^{-1}$ is due to atmospheric CO. The strongest component, C3, is detected in all $^{12}$CO and $^{13}$CO spectra and its emission is centred on BHR 160. The C2 $^{12}$CO emission is distributed in a ridge along the globule centre axis (the line from SW to NE through the centre of the CO map). Emission from the C1 component is detected in the SE edge of the CO map and is visible only in the $^{12}$CO line.

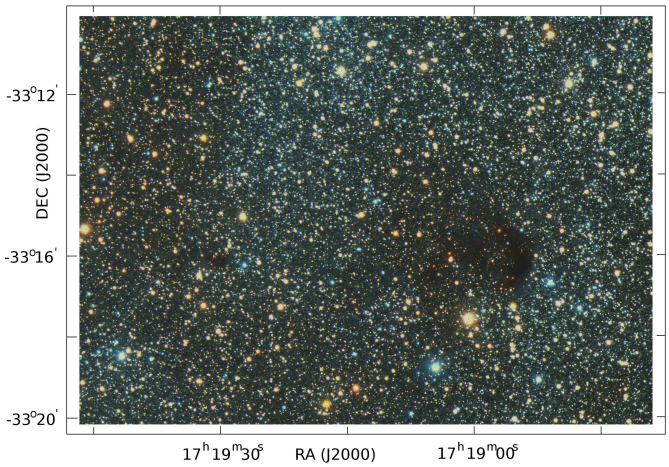


**Fig. 5.** False colour VVV *YZJHK* image.

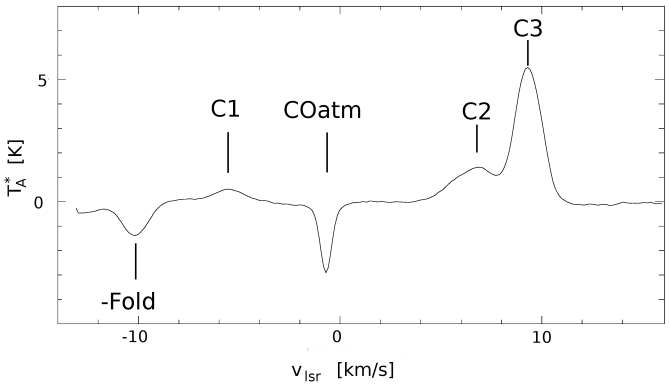


**Fig. 6.** Folded $^{12}$CO (2−1) line (average of spectra around the centre of the map). The three line components, the atmospheric line and the negative component due to the folding process are indicated.

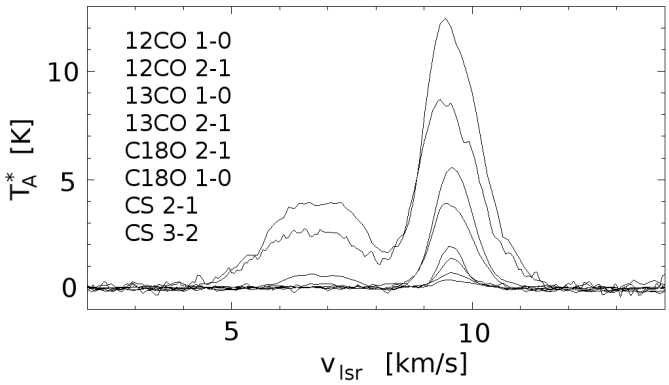


**Fig. 7.** Observed CO and CS lines at the map off-set position +17″, 10″. Only the two strongest line components, C2 and C3, are shown The lines are identified on the left in the order of the intensity of the C3 component.

The CO and CS spectra observed in the off-set map-position +17″, 10″ are shown in Fig. 7. Only components C2 and C3 are shown. Component C3 $^{12}$CO and $^{13}$CO (1−0) line peak velocities are blueshifted with respect to the line peak velocities of the other CO isotopologue and CS lines. This and the slight $^{12}$CO line asymmetry hints at self absorption. The redshifted line wing suggests a weak outflow, but the line shape may also be due to the CO self absorption. Clear emission from the C2 component is seen only in $^{12}$CO and $^{13}$CO lines. The component is broad, flat topped and the blueshifted $^{12}$CO line wing hints at outflowing material.

The contours of component C3 integrated line emission of the three observed CO isotopologues and the two CS transitions are shown in Fig. 8 overlaid on the false colour VVV, H$\alpha$ and Wise 12 $\mu$m images. The CO (1−0) and CS (2−1) contours are white and the CO (2−1) and CS (3−2) contours red. The $^{12}$CO and $^{13}$CO contours cover the whole globule. The integrated line emission in the $^{12}$CO and $^{13}$CO (1−0) transitions is distributed roughly spherically, but in the (2−1) transitions the maximum is closer to BHR 160 IRS1 and the core. Both C$^{18}$O and CS transitions peak near the core. This can be explained by the higher critical densities of these molecules compared to $^{12}$CO. The highest transitions of all the observed molecules have higher critical depth than the lower transitions, and therefore they tend to peak more in the direction of the dense and obscured core. C$^{18}$O and CS molecules are not excited in the low density envelope outside the core. Self absorption in the $^{12}$CO line may also cause suppression of the $^{12}$CO line in the core.

The observed C$^{18}$O (1−0) and (2−1) spectra (in black and red, respectively) in the $T_{\rm A}^*$ scale are shown in Fig. 9. The C$^{18}$O (2−1) emission is stronger in two positions in the core to the south of the map 0, 0 position. As the SEST main beam efficiencies at the C$^{18}$O (1−0) and (2−1) frequencies are 0.70 and 0.50, respectively, the difference in the intensity at these positions would be even higher if expressed in the $T_{\rm MB}$ scale. However, the $T_{\rm MB}$ scale is not useful when observing an extended object which has small scale structure that is smaller than the main beam. The spatial resolution, especially in the C$^{18}$O (1−0) transition (Figs. 8 and 9) is not sufficient to fully resolve the small scale structure in the BHR 160 dense core but at the same time the lower intensity emission is more extended than the main beam. We note that the beams in Fig. 8 indicate HPBW and not the main beam which is larger. Emission is therefore observed not only from the main beam but also from the beam side lobes and the error beam. The SEST beam in the C$^{18}$O (2−1) transition traces better the dense core whereas the beam in the (1−0) transition, with an area four times that in the (2−1), also traces more of the less dense gas in the globule. Direct comparison of the C$^{18}$O (1−0) and (2−1) brightness temperatures is meaningful only if the two transitions trace the same material. A likely explanation for the observed higher $T_{\rm A}^*$ intensity of the C$^{18}$O (2−1) line with respect to the C$^{18}$O (1−0) line in the centre of the core is stronger beam dilution of the lower transition rather than a large difference in the excitation temperature.

The main trend in the distribution of the observed molecules in BHR 160 is that the higher the critical density is, the closer the observed distribution is to the elongated core. Because of the possible line self absorption, the distribution of the $^{12}$CO emission may be misleading.

The channel maps give more detailed information than the line integrals. The $^{12}$CO and $^{13}$CO (2−1) and $^{12}$CO (1−0), $^{13}$CO (1−0), C$^{18}$O (2−1), $^{13}$CO (1−0), CS (3–2) and CS (2−1) channel maps are shown in Fig. 10 and Figs. B.1 to B.6, respectively.

As expected from the line integrals, the strongest $^{12}$CO, $^{13}$CO, and C$^{18}$O (1−0) emission is seen in the direction of the globule centre and the IR source, whereas in the higher observed transitions the maximum emission is shifted towards the globule core.

The C$^{18}$O spectra (Fig. 9) and the C$^{18}$O (2−1) channel map (Fig. B.4), indicate that the maximum intensity which is seen at

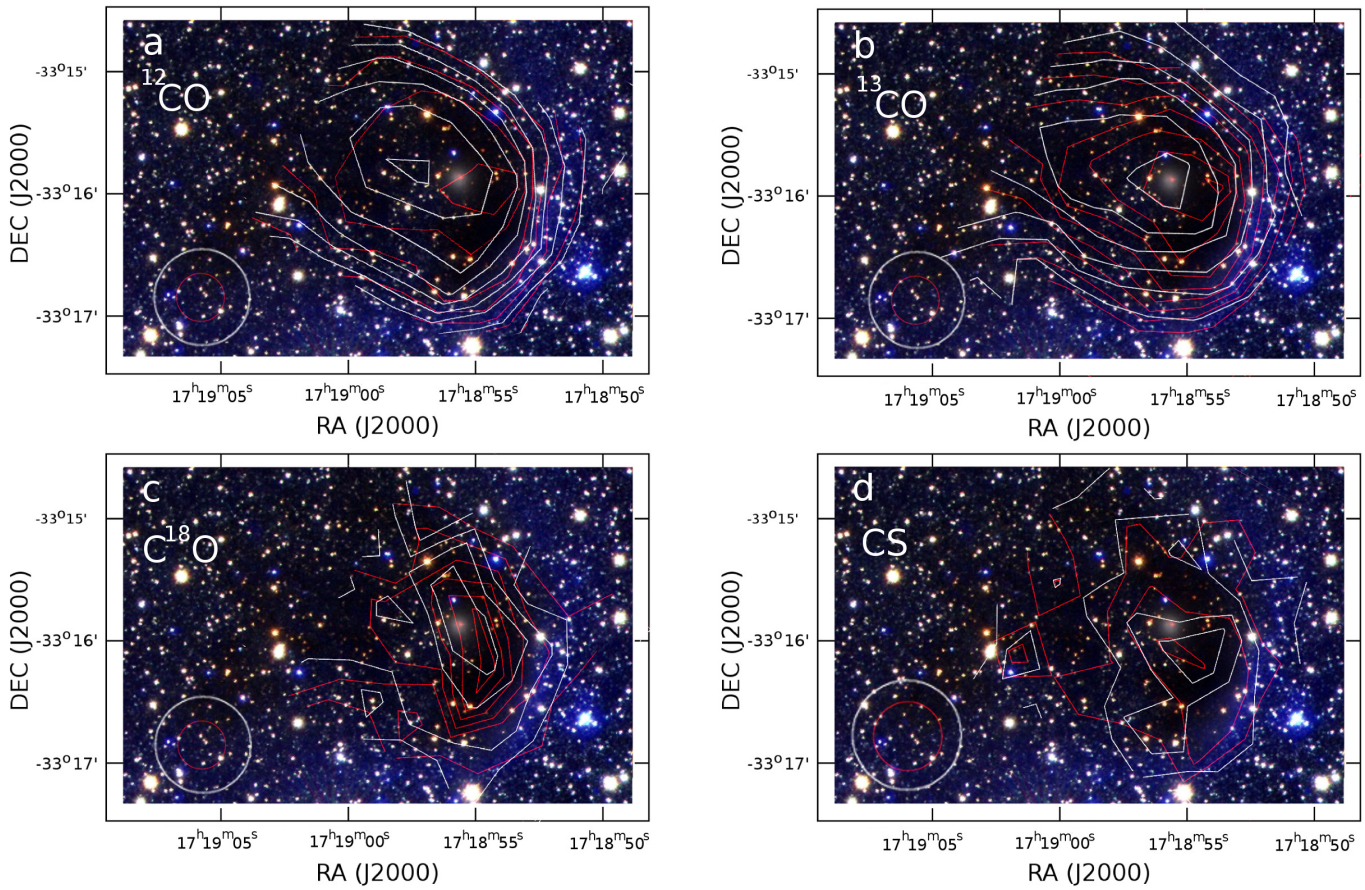


**Fig. 8.** Contours of the line integrals of the observed molecular transitions (only component C3) overlayed on a VVV, H$\alpha$ and WISE false colour image. The respective beam sizes for each molecule are shown in the lower left of each panel. **a)** $^{12}$CO (1−0) (in white) and (2−1) (in red) contours. Lowest contour level and increment in $T_A^*$ scale is 2 K km s$^{-1}$. **b)** As a but for $^{13}$CO. Lowest contour level and increment are 1 K km s$^{-1}$ for $^{13}$CO (1−0) and 0.5 K km s$^{-1}$ for $^{13}$CO (2−1). **c)** As a for C$^{18}$O. Lowest contour level and increment 0.2 K km s$^{-1}$, and **d)** as a for CS (2−1) (in white) and CS (3–2) in red. Lowest contours and increments are 0.2 K km s$^{-1}$ for CS (2−1) and 0.1 K km s$^{-1}$ for CS (3–2).

velocities 9.3 km s$^{-1}$ to 9.75 km s$^{-1}$, lies in the direction of the elongated core between the bright rim and the IR source. The signal-to-noise of the CS spectra is low, but the observed trend is similar to that observed in C$^{18}$O (2−1). The maximum emission in the integrated emission of CS (2−1) and (3–2) lines peaks in the core (Fig. 8c). It is reasonable to assume that the maximum density lies in the direction where the maximum C$^{18}$O (2−1) and CS line emission lies, that is in the direction of the obscured core. The spatial resolution of the present data is not sufficient to define the exact position and extent of the high density region. The maximum is only resolved in C$^{18}$O (2−1) line in the north-south direction but not in the direction perpendicular to it. The dimension of the core in the north-south direction is ∼1′.

The $^{12}$CO and $^{13}$CO channel maps reveal yet another emission line component which emits at velocities between C2 and C3. The emission from this new component is seen in the eastern corner of the mapped area. This line component is not evident in the spectrum in Fig. 6 which is an average of $^{12}$CO (2−1) lines around the centre of the map.

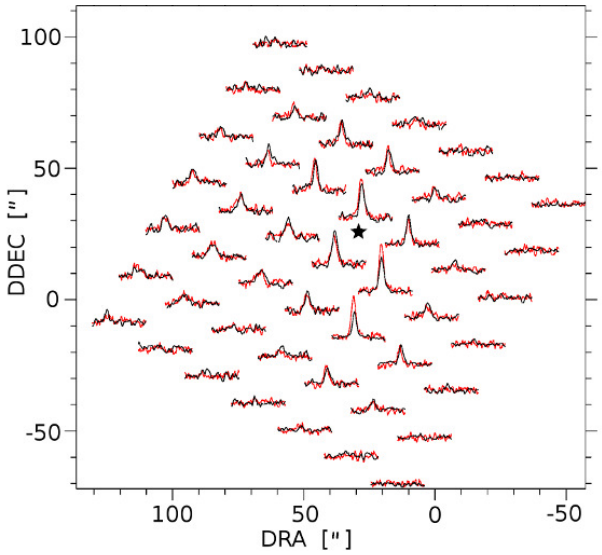


**Fig. 9.** C$^{18}$O (1−0) and (2−1) (in red) spectra observed in BHR 160. The spectra are in the $T_A^*$ scale and the maximum observed C$^{18}$O (2−1) intensity is 1.4 K. The asterisk indicates the position of BHR 160 IRS1.

## 4. Discussion

### 4.1. Extinction

The optical extinction, $A_V$, in the globule and its surroundings can be estimated from the VVV DR2 and 2MASS photometry. A method which is intermediate between the NICE (Lada et al. 1994) and NICER (Lombardi & Alves 2001) methods was used (see Appendix A for details). The extinction, smoothed with a 40″ Gaussian overlayed on the AAO false

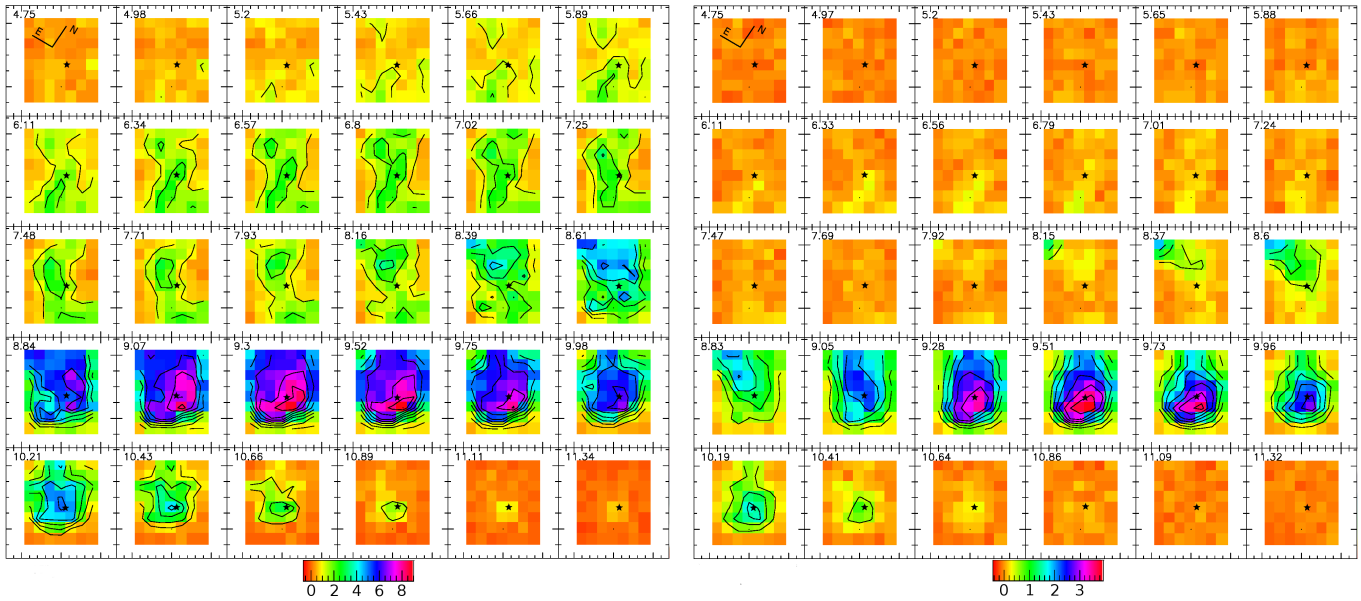


**Fig. 10.** Channel maps of CO (2−1) (on the *left*) and $^{13}$CO (2−1) (on the *right*) line emission in velocity bins of 0.23 km s$^{-1}$. Pixel scale is 20″ by 20″ and the north-east orientation is indicated in the *upper left panel*. The position of BHR 160 IRS1 is indicated by an asterisk in each panel. Lowest contour level and increment is 1.0 K km s$^{-1}$ for $^{12}$CO and 0.5 K km s$^{-1}$ for $^{13}$CO.

colour image, is shown in Fig. A.2. The lowest contour is 5$^{m}$ and the increment is 1$^{m}$. The extinction agrees well with the structures seen in the optical image. Two compact areas are detected corresponding to BHR 160 and BHR 159 10′ to the south of it.

Extinction contours, smoothed with a 30″ Gaussian, in the direction of BHR 160 and overlayed on the VVV, H$\alpha$ and WISE false colour image are shown in Fig. 11. The lowest contour is 5$^{m}$ and the increment is 1$^{m}$. The number of observed stars is low in the direction of the optically most opaque positions in the globule and if the map resolution is increased from 30″, holes will appear into the map. The extinction minimum in the direction of BHR 160 IRS 1 is likely due to high extinction at this position. This minimum is not seen in the large extinction map shown in Fig. A.2 where a 40″ smoothing Gaussian was applied. The extinction agrees both with the obscuration seen in Fig. 11 and with the observed distribution of molecular line emission (Fig. 8).

The extinction reveals an elongated Appendix to the east of the globule main body. The extinction map is a two dimensional projection and traces the material along the line of sight. As BHR 160 is apparently associated with an extended compressed shell of a distant extinct HII region it is not unlikely that other structures in the shell are seen in projection in the same direction. Unlike extinction, the spectral line maps have an additional dimension, namely the velocity. The distribution of the emission from the C3 CO line component centred at 9.5 km s$^{-1}$ is well correlated with the optical appearance of the main globule. As noted in Sect. 3.2 there is indication of emission at velocities between the C2 and C3 components in the $^{12}$CO and $^{13}$CO channel maps in the upper left corner of the panels. This corresponds to the very east corner of the mapped area adjacent to the Appendix. The $^{13}$CO (1−0) and (2−1) spectra in offset positions 0″, 0″ and +135″, 10″ are shown in Fig. B.7. The figure indicates that there is a separate velocity component centred at 8.5 km s$^{-1}$ between components C2 and C3. The emission at 8.5 km s$^{-1}$ coincides with the western edge of the Appendix. The elongated cometary-like structures in the region (Figs. 2 and 3) all face towards the O star HD 155806. However, different from this, the orientation of the appendix and BHR 160 complex is elongated in the east-west direction. We argue thus that the Appendix is not connected to BHR 160 but is a separate structure seen in projection.

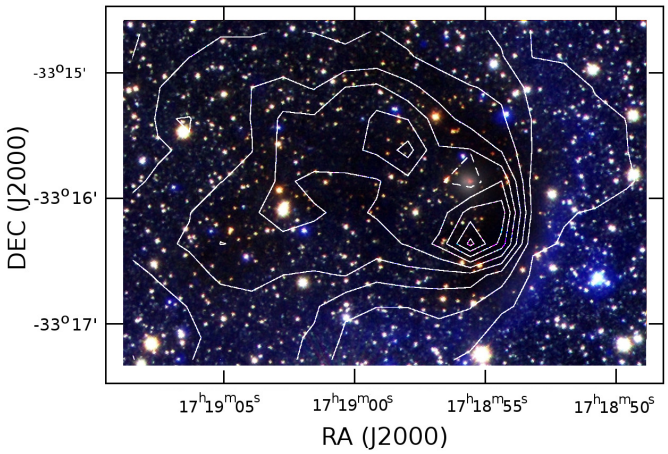


**Fig. 11.** As Fig. 8 with optical extinction contours overplotted. The contours start at 5$^{m}$0 and the increment is 1$^{m}$.

### 4.2. The mass of BHR 160

The cloud mass can be estimated from the observed C$^{18}$O line emission. Assuming LTE, an optically thin line and C$^{18}$O abundance of $2.0\times10^{-7}$, the maximum $H_2$ column density averaged over the SEST 23″ beam in the core is $4.4\times10^{22}$ cm$^{-2}$ if the C$^{18}$O excitation temperature is 10 K, and $3.7\times10^{22}$ cm$^{-2}$ if the temperature is 15−30 K. Assuming LTE, an excitation temperature of 10 K and an average molecular weight of 2.8 per $H_2$ molecule, the total integrated mass of the globule summed up from the C$^{18}$O observations is 100 $M_\odot$ $(d/1.6\,\mathrm{kpc})^2$ where $d$ is the distance to the globule. Approximately 70% of the mass lies in the dense core. If the excitation temperature is higher, 15 to 30 K, the values are 10% lower. Besides the distance and excitation temperature also variations in the line optical depth and

deviation from LTE cause further uncertainty to the mass estimation. A conservative estimate of the accuracy of the mass is ±50%. This mass refers also only to the molecular gas as traced by $C^{18}O$ in the mapped area. The dense cloud core is surrounded by an extended less tenuous envelope where $C^{18}O$ is not excited.

The optical extinction estimated from the VVV photometry offers an independent check on the $H_2$ column density. Unlike molecular line or dust thermal emission, the extinction depends only on dust column density and not on gas/dust temperature nor density. The maximum observed optical extinction for a single star in the core estimated from the VVV data is $20^m \pm 4^m$. This value is a lower limit for the core maximum extinction as no stars are seen through the very centre of the core. Using the relation between the hydrogen column density and extinction in Bohlin et al. (1978), the estimated $H_2$ column density corresponding to this extinction is approximately $2.0 \pm 0.4 \times 10^{22}$ cm$^{-2}$ ($Av/E(B-V)$ is assumed to be 3.2). This is slightly lower than that derived in the centre of the core from the $C^{18}O$ data. The mass of the globule within the extinction contours of $7^m$ in Fig. 11 is $210 \pm 80(d/1.6\,\mathrm{kpc})^2\,M_\odot$. The area is larger than that covered by the molecular line observations. Divided between the appendix (area east of $17^h19^m$ and south of $-33°15'20''$) and the globule the masses are $80 \pm 30\,M_\odot(d/1.6\,\mathrm{kpc})^2$ and $130 \pm 50\,M_\odot(d/1.6\,\mathrm{kpc})^2$, respectively. Here it is assumed that the Gaussian smoothed extinction is accurate to $3.0^m$ in the direction of the globule and $2.0^m$ in the appendix (chiefly Fig. A.4).

We have also done radiative transfer modelling using the Monte Carlo method (Juvela 1997) assuming a centrally condensed, spherically symmetric geometry. Even though the core is clearly elongated, the modelling should give an indication of the possible $H_2$ densities and the excitation temperature in the core. Only the C3 line component and the least optically thin lines, $C^{18}O$ (2−1)/(1−0) and lines tracing density (CS (3–2)/(2−1)) were considered. The excitation temperature in the centre of the core had to be raised to 40 K to explain the observed $C^{18}O$ (2−1)/(1−0) line ratio. In the outer parts, the temperature dropped to 20 K. The model which could reproduce the observed $C^{18}O$ and CS lines had a central density of $3 \times 10^4$ cm$^{-3}$ which rapidly decreased and was less than 1000 cm$^{-3}$ at the edges. The total mass of such a model is 100 $M_\odot$. These values are in line with those derived from the LTE approximation. However, this should be only considered to demonstrate that it is possible to construct a hypothetical cloud core which reproduces the observed line intensities using similar input values as those derived from the LTE approximation.

### 4.3. Star formation

The only IR excess source detected so far within BHR 160 is IRS1 (WISE J171855.54-331554.3). We have used the spectral energy distribution (SED) fitting tool of Robitaille et al. (2007) to fit the WISE MIR and IRAS FIR data (Fig. 12). As the IRAS 100 $\mu$m flux is likely to contain emission from the globule dense core, it is given as an upper limit. The data wavelength range is not sufficient for a unique fit but the results point to a Class I protostar. The fitted stellar temperature is 4400 K, with masses and luminosity range between 1.5 and 2.5 $M_\odot$ and 70 to 200 $L_\odot$. However, even a five $M_\odot$ high mass star is suggested by one fit.

SED fits were also made for the seven additional stellar sources marked in Fig. 4. No *JHK*s measurements are available for source 7 as it is not visible even in the VVV data so only WISE data are used. 2MASS photometry was used for the remaining sources because the stars are saturated in the VVV photometry. As in the case of BHR 160 IRS1, no unique fit is possible for most of the sources, but the fits are sufficient to demonstrate that the objects are likely to be young stars with a dust shell and/or disk. Even though the fitted values should be considered only as indicative, the result is sufficient to show that active star formation is taking place in the region. The results of the fits are listed in Table 2 and plotted in Fig. B.8. It would be possible to fit most of the sources assuming strong interstellar reddening only, but in that case the distance to the stars would have to be less than 20 pc. The fitted $A_V$ of $15^m$ to $30^m$ is not plausible for such nearby sources.

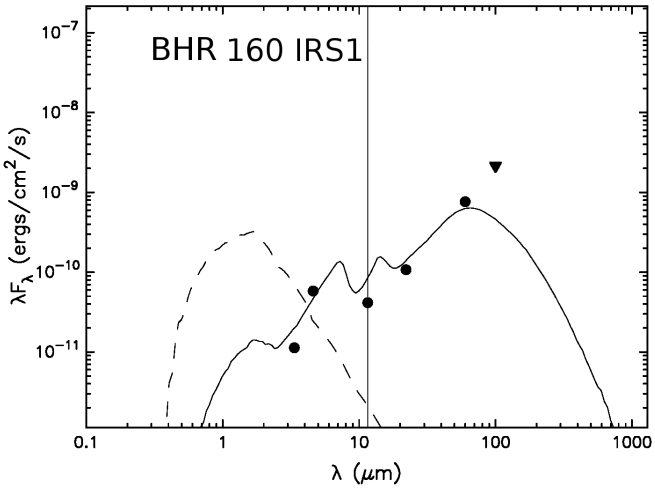


**Fig. 12.** SED fit to BHR 160 IRS1 WISE and IRAS data. The IRAS 100 $\mu$m value is an upper limit. The continuous line shows the fit and the dashed line the SED of the unreddened central source.

**Table 2.** SED fits.

| Star | WISE | $T$ ($\times 10^3$ K) | $M$ ($M_\odot$) | $L$ ($L_\odot$) |
|---|---|---|---|---|
| 1 | J171855.54–331554.3 | 4.4 | 1.8–5.6 | 70–200 |
| 2 | J171917.36–331941.3 | 15–20 | 4.8–6.5 | 930–1500 |
| 3 | J171913.86–331917.7 | 18–26 | 5.0–10.0 | 1000–2000 |
| 4 | J171900.44–331734.9 | 25 | 9.6 | 5500 |
| 5 | J171855.17–331716.0 | 15 | 4.5–5.5 | 2700–4000 |
| 6 | J171854.59–331747.9 | 15 | 4.4 | 2500 |
| 7 | J171833.24–331538.6 | 4 | 0.7-2 | 10–30 |
| 8 | J171833.26–331538.5 | 25 | 9.7 | 5500 |

BHR 160 IRS1 is associated with a dense circumstellar envelope. It is, however, not clear how much the BHR 160 IRS1 IRAS fluxes are contaminated by the adjacent globule core. Except for star 7, the remaining stars in Table 2 are hotter, much more luminous and have higher mass ($M > 4\,M_\odot$) than BHR 160 IRS1. The projected distance on the sky between BHR 160 IRS1 and the fitted stars is between 0.5 and 2.4 pc. It is likely that the stars are also newly formed out of the remnant neutral material surrounding the Sco OB4 association.

### 4.4. Bright rim

The intense bright rim, catalogued as Magakian 714 (Magakian 2003), that is associated with BHR 160 is very rare among cometary globules. The only case that we are aware of with

a similar intense bright rim is the globule CG 1 in the Gum Nebula, which is illuminated by the young Herbig Ae/Be star NX Pup = Cod–44°3318, born within the globule (Reipurth 1983; Haikala et al. 2010). We here consider the relationship between BHR 160 and HD 319648, which is located just 30″ in front of the globule.

Noel Cramer of Geneva Observatory has kindly obtained Geneva photometry of HD 319648, and using the calibrations of Cramer (1993) he has derived the following parameters: $m_V$ = 10.593, $M_V$ = −1.7, $A_V$ = 1.18, distance 1.64 kpc, and a spectral type of B3III. The distance is in excellent agreement with the distance of 1.61 kpc derived by Persi & Tapia (2008) for the nearby NGC 6334 cluster, which is assumed to be also part of the Sco OB4 association (Roslund 1966). The spectral type indicates that the star has enough UV radiation to form a photoionized region in the Magakian 714 bright rim. The projected separation of HD 319648 and the bright rim is only 0.23 pc. We thus consider it highly likely that the globule and the star are located close to each other, and that their closeness in the sky is not just a line-of-sight effect. The question is then whether HD 319648 was born in the globule or just is passing by the globule. Cases of random encounters between stars and globules are known, a fine case is the globule CG13 in the Gum Nebula, which has encountered a star passing through it (Reipurth 1983).

HD 319648 is clearly a member of the Sco OB4 association (Roslund 1966) but could have been formed elsewhere in the association and by chance moved into the vicinity of BHR 160. The mean velocity dispersion of OB stars in Sco OB4 is ∼7 km s$^{-1}$ (Roslund 1969), and a lower limit to the time HD 319648 could have been in the vicinity of the globule comes from dividing the length of the bright rim (∼2′) with this velocity, which yields a time span of 130 000 yr. Since the Sco OB4 association must be at least several million years old, it is certainly possible that one of the association members during that time has wandered into the vicinity of BHR 160. However, the fact that the star is placed right in front of the globule suggests to us that it may have formed in the globule as a secondary star formation event, probably triggered by the massive O star HD 155806, which is also located along the main axis of the globule. We may therefore be witnessing a case of sequential star formation, where the formation of HD 319648 was triggered by HD 155806, while HD 319648 in turn may have triggered the formation of the currently embedded source IRS 1 within the globule.

### 4.5. Cloud structure

Biologically BHR 160 is a scaled up version of the head of the archetype cometary globule CG 1 (Hawarden & Brand 1976; Reipurth 1983) in the Gum Nebula. The CG 1 bright rimmed head has a diameter of a few arcminutes and is illuminated by the nearby pre-main-sequence star NX Pup, and a protostar, CG 1 IRS 1, is situated at the side of the elongated core (Haikala et al. 2010). The total C$^{18}$O mass of the CG 1 core is, however, only a tenth of that measured in BHR 160. And another difference is that CG 1 IRS1 is situated between the illuminating star and the core whereas in BHR 160 the protostar is on the opposite side of the core. The similarities in the morphology and the location of these two globules at the edge of a large, well evolved HII region suggest a similar origin. In Mäkelä & Haikala (2013) it was argued that the formation of CG 1 was driven by radiation induced implosion (Reipurth 1983). Less dense material extends to NE from the dense BHR 160 core, but there is no indication in Fig. A.2 that the globule has a long tail like that of CG 1. The cometary globule (known as BHR 159) just south of BHR 160 also points at similar processes being active here and in the Gum Nebula.

## 5. Summary and conclusions

We have carried out dedicated molecular line observations in the CO (and isotopologues) (1−0), (2−1) and in CS (2−1) and (3–2) transitions to study the basic properties of the bright rimmed dark cloud BHR 160. Combining these data with data available in various public surveys provides insight into the globule and its surroundings:

1. AAO/UKST imaging in the H$\alpha$ line reveals that BHR 160 is part of the shell of an extinct HII region. Besides BHR 160 several other globules are associated with the same shell of neutral material at the edge of the Sco OB4 association.
2. BHR 160 is elongated with dimensions of approximately 5′ × 3′. The globule is delineated on three sides by a halo emitting in the H$\alpha$ line while a cometary-like tail is present on the NE side.
3. The 1′ by 0.′6 BHR 160 core is dense and bound sharply in the west by the bright H$\alpha$ rim which is also seen faintly in reflected light at other wavelengths.
4. The maximum $H_2$ column density in the globule core is $4.4 \times 10^{22}$ cm$^{-2}$ as estimated from the C$^{18}$O data, or half of this when estimated from extinction. Mass estimated from the C$^{18}$O observations using LTE approximation within the mapped region is $100 \pm 50(d/1.6\,\mathrm{kpc})^2\ M_\odot$ of which 70% is contained in the core. The total BHR 160 mass estimated from optical extinction is $210 \pm 80(d/1.6\,\mathrm{kpc})^2\ M_\odot$. Approximately 40% of the total optical mass is contained in the BHR 160 appendix which is argued to be a separate cloud seen in projection.
5. Only one infrared excess star, BHR 160 IRS1, was detected within BHR 160. It lies off the core on the opposite side to the bright rim. Only a faint slightly extended object is seen in the VVV *Ks* image but the star is seen in all the four WISE channels from 3.4 $\mu$m to 20 $\mu$m. An IRAS source lies nominally 15″ to the west of IRS 1, but in the HIRES enhanced IRAS 60 $\mu$m image the emission maximum coincides with IRS 1. A SED fit to the WISE and IRAS 60 $\mu$m fluxes points at a low mass Class I protostar of about 2 $M_\odot$. Other fits from subsolar up to 5 $M_\odot$ are, however, possible and the fits must be considered only indicative until better FIR data become available.
6. Analysis of seven bright stellar WISE sources seen towards BHR 160 provides evidence for recent star-formation in the region. According to SED fits to *JHK*s and WISE data, six of these are high mass objects in different stages of early stellar evolution. Only one low mass source is detected, but only the WISE fluxes are available for this star. As all the fits are based on a restricted wavelength range they should all be considered as indicative.

*Acknowledgements.* We thank Noel Cramer for obtaining the Geneva photometry of HD 319648, and Bambang Hidayat for sending us a copy of the Thé (1961) paper. This research has made use of the following resources: data products from observations made with ESO Telescopes at the La Silla or Paranal Observatories under ESO programme ID 179.B-2002; SIMBAD database, operated at CDS, Strasbourg, France; NASA's Astrophysics Data System Bibliographic Services; data from the Southern H$\alpha$ Sky Survey Atlas (SHASSA), which was produced with support from the National Science Foundation; data products from the 2MASS, which is a joint project of the University of Massachusetts and the Infrared Processing and Analysis Center/California Institute of Technology, funded by the NASA and the US National Science Foundation; data products from the Wide-field Infrared Survey Explorer, which is a joint project of the University of

California, Los Angeles, and the Jet Propulsion Laboratory/California Institute of Technology, funded by the National Aeronautics and Space Administration.

## References

Auman, H., Fowler, J., & Melnyk, M. 1990, AJ, 99, 1674
Bohlin, R. C., Savage, B. D., & Drake, J. F. 1978, ApJ, 224, 132
Bok, B. J. 1977, PASP, 89, 597
Bourke, T. L., Hyland, A. R., & Robinson, G. 1995a, MNRAS, 276, 1052
Bourke, T. L., Hyland, A. R., Robinson, G., James, S. D., & Wright, C. M. 1995b, MNRAS, 276, 1067
Cramer, N. 1993, A&A, 269, 457
Foster, J. B., Román-Zúñiga, C. G., Goodman, A. A., Lada, E. A., & Alves, J. 2008, ApJ, 674, 831
Fullerton, A. W., Petit, V., Bagnulo, S., Wade, G. A., & Wade. 2011, in IAU Symp. 272, eds. C. Neiner, G. Wade, G. Meynet, & G. Peters, 182
Haikala, L. K., & Reipurth, B. 2010, A&A, 510, A1
Haikala, L. K., Mäkelä, M. M., & Väisänen, P. 2010, A&A, 522, A106
Hartley, M., Tritton, S. B., Manchester, R. N., Smith, R. M., & Goss, W. M. 1986, A&AS, 63, 27
Hawarden, T., & Brand, P. 1976, MNRAS, 175, 19
Juvela, M. 1997, A&A, 322, 943
Lada, C., Lada, E., Clemens, D., & Bally, J. 1994, ApJ, 429, 694
Lombardi, M., & Alves, J. 2001, A&A, 377, 1023
Magakian, T. Y. 2003, A&A, 399, 141
Mäkelä, M. M., & Haikala, L. K. 2013, A&A, 550, A83
Parker, Q. A., Phillipps, S., Pierce, M. J., et al. 2005, MNRAS, 362, 689
Persi, P., & Tapia, M. 2008, in Handbook of Star Forming Regions, Vol. II, ed. Bo Reipurth, ASP, 456
Reipurth, B. 1983, A&A, 117, 183
Reipurth, B. 2008, in Handbook of Star Forming Regions, Vol. II, ed. Bo Reipurth, ASP, 847
Robitaille, T. P., Whitney, B. A., Indebetouw, R., & Wood, K. 2007, ApJS, 169, 328
Roslund, C. 1966, Arkiv för Astronomi, 4, 101
Roslund, C. 1969, Arkiv för Astronomi, 5, 209
Saito, R. K., Hempel, M., Minniti, D., et al. 2012, A&A, 537, A107
Thé, P.-S. 1961, Contributions from the Bosscha Observervatory, 12
Walborn, N. R. 1973, AJ, 78, 1067
Wright, E. L., Eisenhardt, P. R. M., Mainzer, A. K., et al. 2010, AJ, 140, 1868

## Appendix A: Estimation of the extinction: SIMPLE

The spread of the $(J-H)$ and $(H-\mathrm{K})$ colour indices of unreddened main main sequence stars is small, being approximately $0\overset{\mathrm{m}}{.}7$ and $0\overset{\mathrm{m}}{.}5$, respectively. For the giant branch the spread of the $(H-K)$ index is even smaller ($0\overset{\mathrm{m}}{.}3$). Interstellar reddening increases both colour indices by an amount which is proportional to the amount of the reddening. If the reddening law is known it is possible to estimate the reddening affecting each measured star from its position relative to the unreddened main or giant sequence. A similar method was used traditionally for example when estimating the interstellar reddening of stars using the *UBV*colour−colour diagram. When the near-infrared (NIR) photometry was conducted using a single pixel detector it was possible to estimate the reddening of each observed star manually. However, the number of stars detected using modern NIR arrays is so large that estimating the reddening manually star by star is not feasible and a more automated method must be applied.

Lada et al. (1994) introduced the NICE (Near Infra Red Excess) method to automatically estimate the the reddenings from stellar NIR colours using the observed $(H-K)$ colour index. Intrinsic $(H-K)_0$ values are estimated from the colour distribution of the stellar population in a non-reddened control field near the programme field. Any deviation from the intrinsic colour is attributed to reddening. The Near Infra Red Excess Revisited (NICER) method (Lombardi & Alves 2001) utilises both the $(J-H)$ and $(H-K)$ colour indices. In addition to intrinsic $(H-K)_0$ and $(J-H)_0$ indices also the colour distribution of the stellar population is estimated using a non reddened control field. The NICE and NICER provide the difference in reddening between the programme and control fields. For a summary of the two methods see Lombardi & Alves (2001).

NICE or NICER methods work best when observing nearby dark clouds off the Galactic plane where the interstellar reddening outside the cloud is small. Both methods are problematic if the programme field lies in a direction which contains many dust clouds, possibly both in front and behind the object, and no nearby unreddened control field can be found. This is typically the case especially in or near the Galactic plane in the general direction of the Galactic centre.

BHR 160 lies near the Galactic plane only ∼7° from the centre ($l$ = 353.2518°, $b$ = +02.4154°) at a distance of 1.6 kpc. Any line of sight in this direction is bound to contain unrelated molecular clouds and diffuse ISM. No nearby unreddened control field could be found. Therefore a robust method, which is basically automatising the traditional method of estimating reddenings from the *JHK*s colour−colour diagram was applied. This method, which we call SIMPLE, is less sophisticated than the NICER method but is sufficient for the purpose of this paper.

Contrary to NICER the zero point for the reddening is assumed, not estimated from the distribution of stars in a control field. A $(J-H)_0$–$(H-K)_0$ value $0\overset{\mathrm{m}}{.}8$, $0\overset{\mathrm{m}}{.}16$ below the unreddened late main sequence which is typical for an unreddened Galactic stellar field was adopted. The actual field stellar population depends on the Galactic line of sight (Galactic pole, anti-centre, centre or intermediate) which leads to an additional error source as compared with the NICER method. The reddening for each star is estimated as in the NICER method and corresponds to the distance from the star along the reddening line to a line perpendicular to this, the zero line, which goes through the adopted $(J-H)_0$–$(H-K)_0$ position. It is impossible to decide only from stellar *JHK*s colours if a star is a late-type main sequence star or an early-type star. The stars below the zero line are, however, likely to be early type stars. Instead of zeroing their reddening they are assumed to originate from the earlier main sequence and their reddening is estimated. The reddening for stars near the unreddened early main sequence was set to zero. The imaged area is divided into bins where the reddening is estimated as the Gaussian weighted median of stars near the selected position. If only one or no stars is found the pixel is blanked. The adopted pixel size is half the Gaussian half width. The estimate is the average extinction in the pixel and can be much smaller than the maximum extinction detected in it.

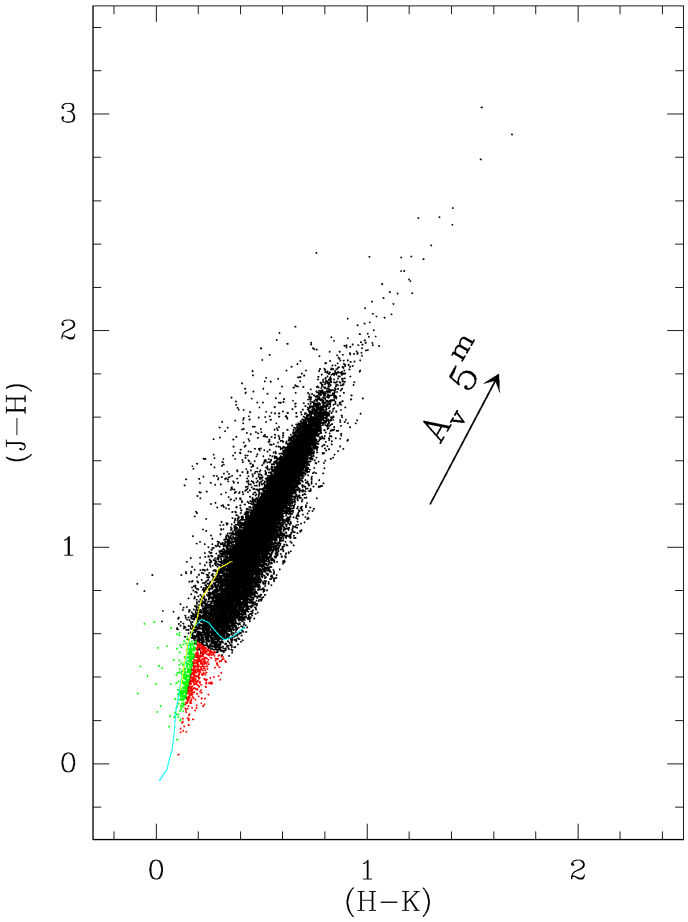


**Fig. A.1.** *J–H*, *H–K* colour−colour diagram of the VVV stars in Fig. 5 fullfilling the selection criteria. The blue and yellow curves indicate the locations of unreddened dwarf and giant stars. The arrow indicates the effect of $5^{\mathrm{m}}$ of reddening. The stars assumed to be unreddened main sequence stars and the assumed reddened early type stars below the late main sequense are plotted in green and red, respectively

To estimate the interstellar reddening in the direction of BHR 160 using the VVV data base, objects classified as stars (VVV "merged class 1") detected in all *JHK*s bands and with a magnitude error less than $0\overset{\mathrm{m}}{.}2$ were included. In addition VVV stars fainter than $17^{\mathrm{m}}$ in $J$ band were excluded and stars brighter than $12^{\mathrm{m}}$ in $J$ band were replaced by 2MASS photometry. Only stars within or near the reddening line were used. This selects stars with intrinsic colours similar to main sequence stars and giants and eliminates outliers which consist mainly of stars with strong NIR excess and a variety of evolved stars, galaxies and AGNs (see for example Foster et al. 2008). The number of objects in the area imaged in Fig. 3 and full-filling these requirements is 51 000. The $(J-H)$–$(H-K)$ colour−colour diagram of the selected stars is shown in Fig. A.1. The stars in the three regions described above are colour coded by green (zero reddening

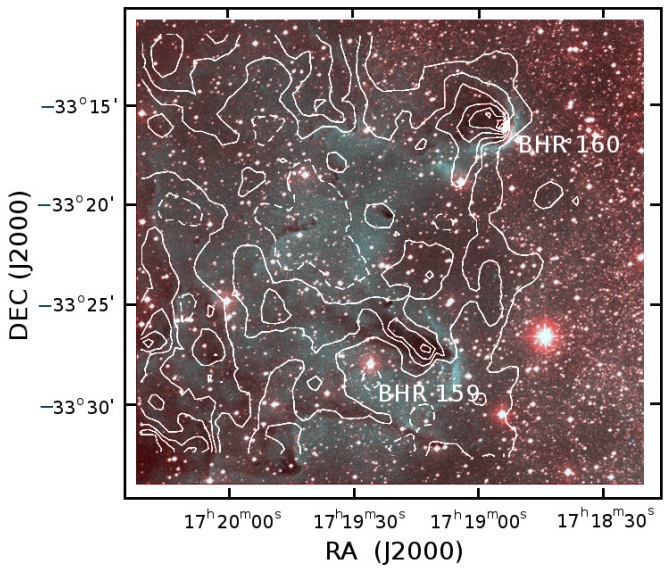


**Fig. A.2.** As Fig. 3 with extinction contours overlayed. The contours range from $5^m$ to $12^m$ in steps of $1^m.0$.

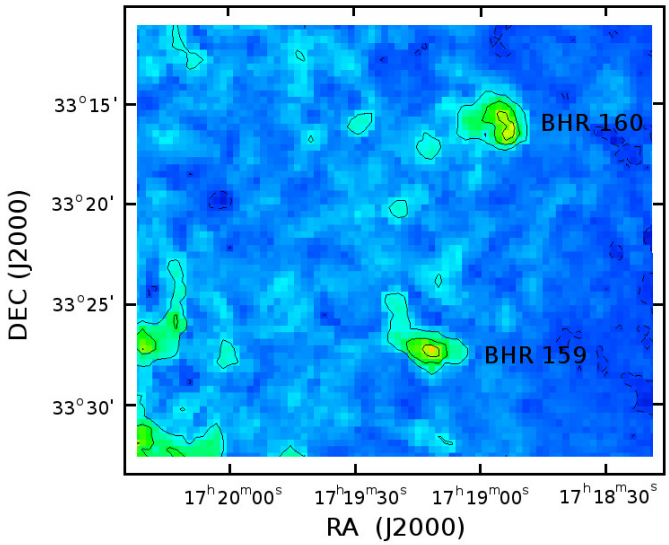


**Fig. A.3.** Noise estimate for the extinctions in Fig. A.2. The contours range from $1^m$ (dashed) to $4^m$ in steps of $1^m.0$.

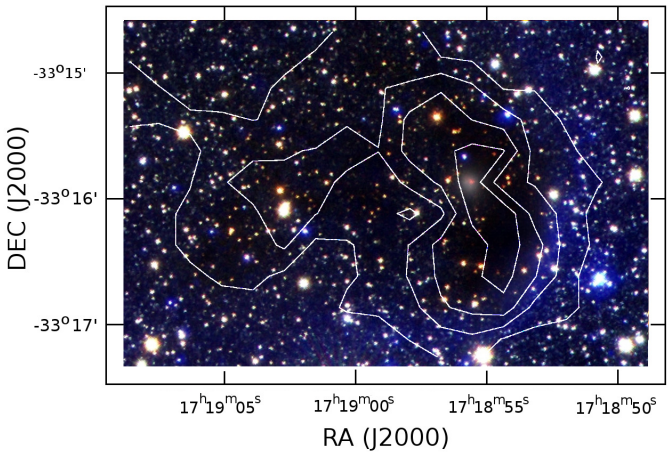


**Fig. A.4.** Noise estimate for the extinctions in Fig. 11. The contours range from $2^m$ to $5^m$ in steps of $1^m.0$.

stars near the main sequence), red (early type stars below the late main sequence) and black (stars in or near the reddening line).

Almost any pixel in the area being studied contains stars with zero or near zero reddenings and also reddenings significantly larger than the average. The standard deviation of reddenings included into the average is thus large and applying sigma clip would mask both the near zero and the large reddenings. However, the large reddenings in the inspected area are most probably correct and trace the densest clumps in the area. Masking these stars would therefore result in underestimating reddening in the clouds. Therefore instead of applying sigma-clip it was decided only to mask the reddenings clearly smaller than the median of the stars in each pixel. BHR 160 lies 1.6 kpc away and the near zero reddenings trace the nearby stars. Because of this choice the resulting rms (noise estimate) of reddenings is large in directions to the dense clumps in the region. The calculated noise estimates in the area of Fig. A.2 is shown in Fig. A.3. The estimated noise is below two magnitudes over most of the image area and as expected, rises in the regions of high extinction. The locations of high extinction tend to stand out from the surroundings better in the noise images than in the extinction images. The noise is highest in the direction of BHR 159 and BHR 160.

The accuracy of the derived reddening distributions depends mainly on the limiting magnitude of the stellar photometry data and stellar density in the programme field. The lower the limiting magnitude the lower is the maximum reddening that one can detect. The spatial resolution of the derived reddening distribution is proportional to the stellar density. The more stars are observed per square arcminute the smaller the selected pixel size can be. The accuracy of the resulting reddening distribution is a combination of these two effects. The maximum possible spatial resolution and the accuracy of the reddening distribution varies within the field. The noise estimate (Fig. A.3) is low in areas of low extinction as many stars are detected per pixel (Fig. A.1). Because of the high extinction in the direction of BHR 159 and BHR 160 only few stars can be seen through the centres of the globules. The reddening is too high for the distant late main sequence stars to be detected (limiting magnitude of the photometric data) through the globules and thus the nose estimate is high. Only few highly reddened stars can be seen. When the extinction is too high no background stars can be seen. This is probably the case in the direction of BHR 160 IRS1 where a local minimum is seen in the reddening distribution (Fig. 11). The number of stars in the colour−colour diagram in Fig. A.1 decreases significantly when the estimated extinction is nine magnitudes or more. The areas in Figs. 11 and A.2 where the extinction is higher than $9^m$ are likely to be lower limits.

## Appendix B: Additional figures

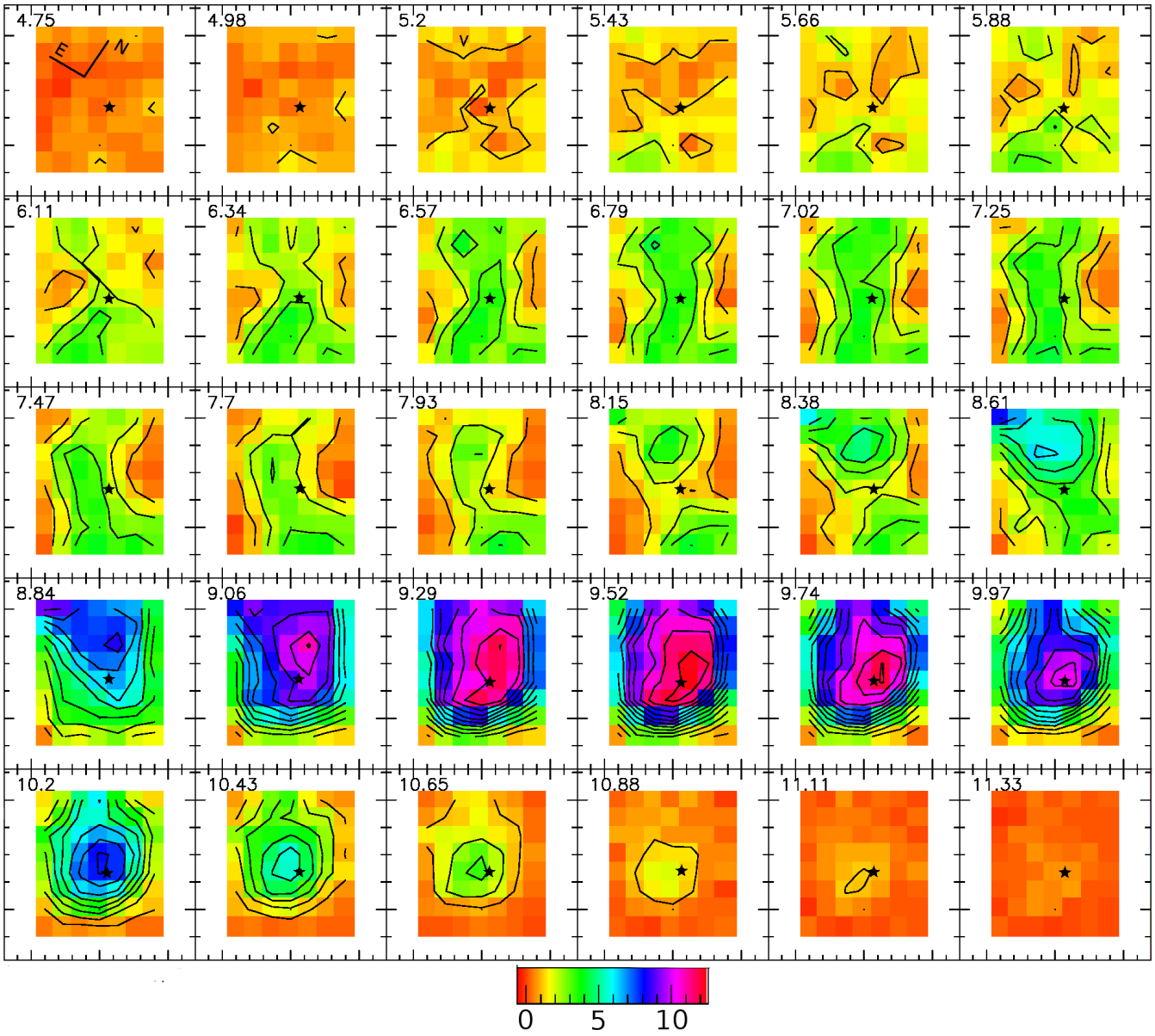


**Fig. B.1.** Channel map of CO (1−0) line emission in velocity bins of 0.23 km s$^{-1}$. Pixel scale is 20″ by 20″ and the north-east orientation is indicated in the *upper left panel*. The position of BHR 160 IRS1 is indicated by an asterisk in each panel. The lowest contour level and increment are 1.0 K km s$^{-1}$.

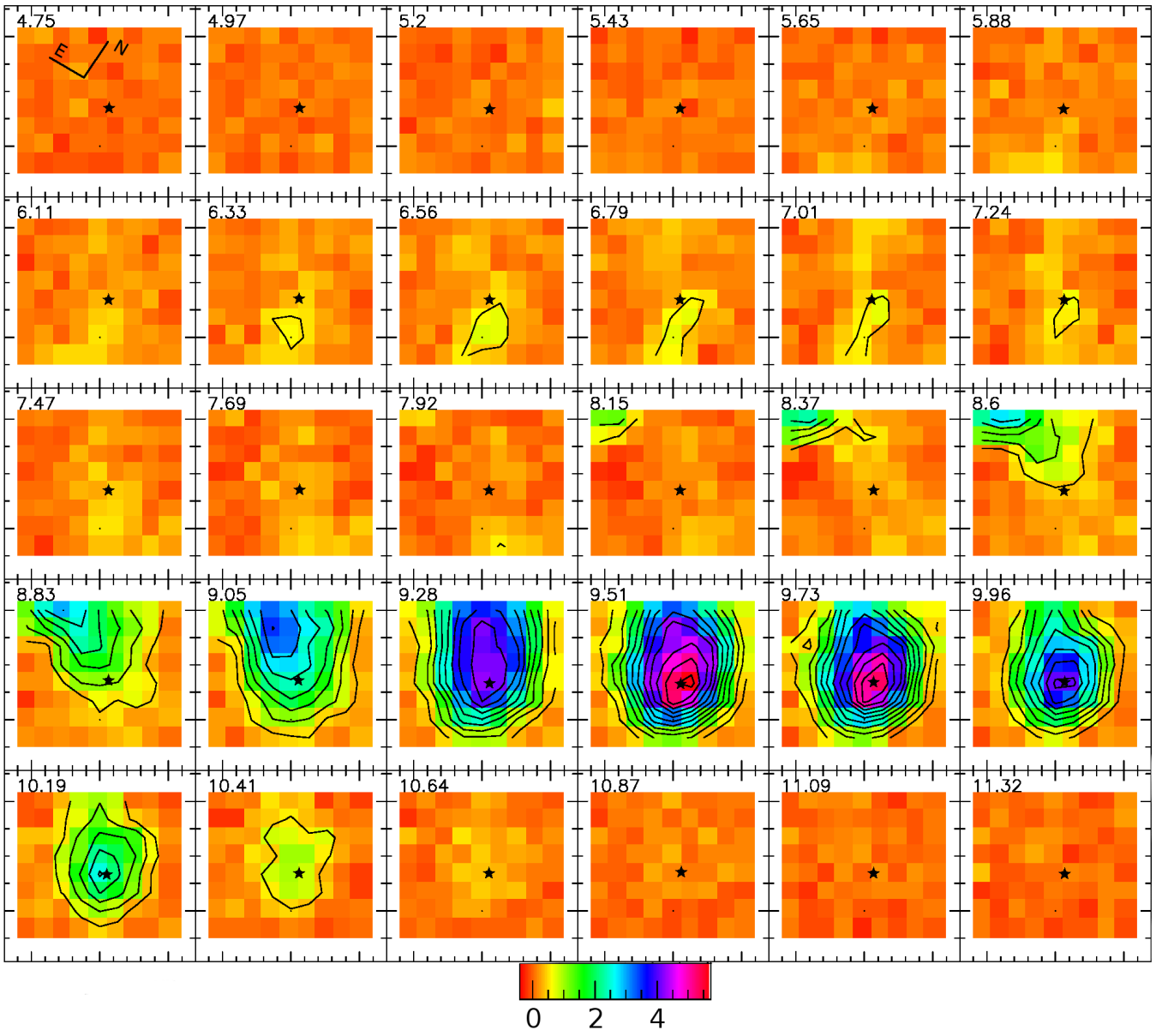


**Fig. B.2.** As Fig. B.1 for $^{13}$CO (1−0). The lowest contour level and increment are 0.5 K km s$^{-1}$.

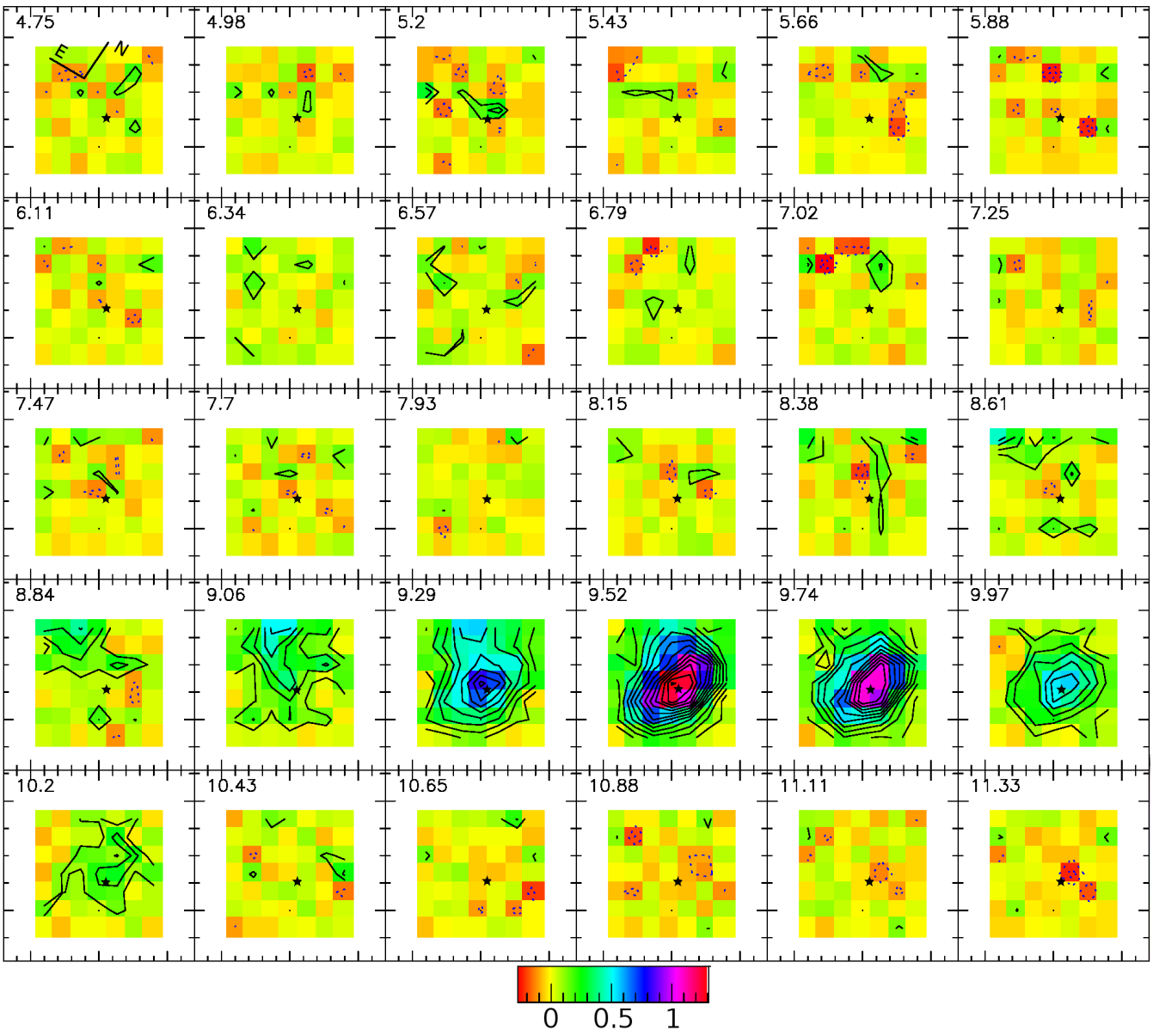


**Fig. B.3.** As Fig. B.1 for $C^{18}O$ (1−0). The lowest contour level and increment are 0.1 K km s$^{-1}$.

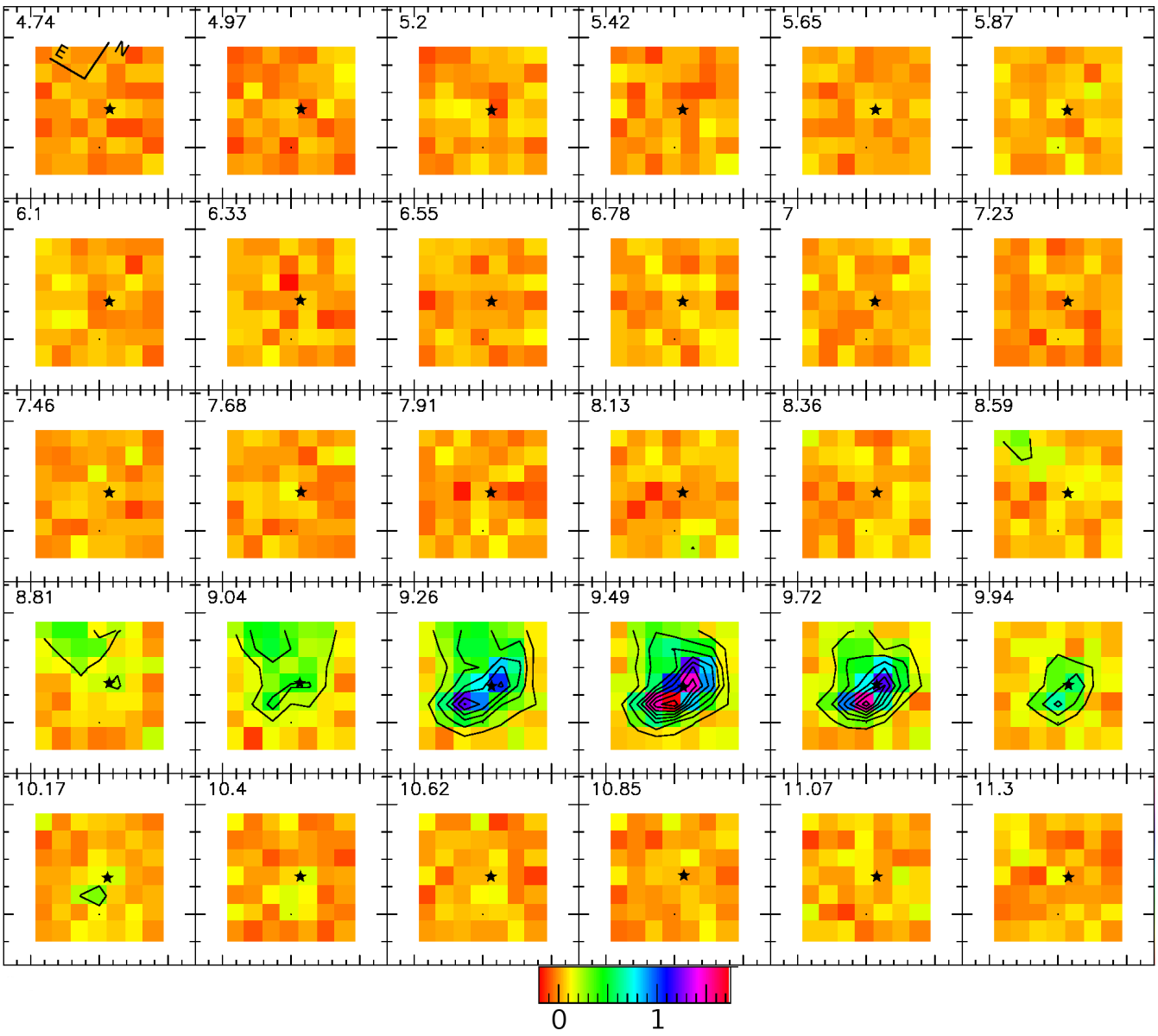


**Fig. B.4.** As Fig. B.1 for $C^{18}O$ (2−1). The lowest contour level and increment are 0.2 K km s$^{-1}$.

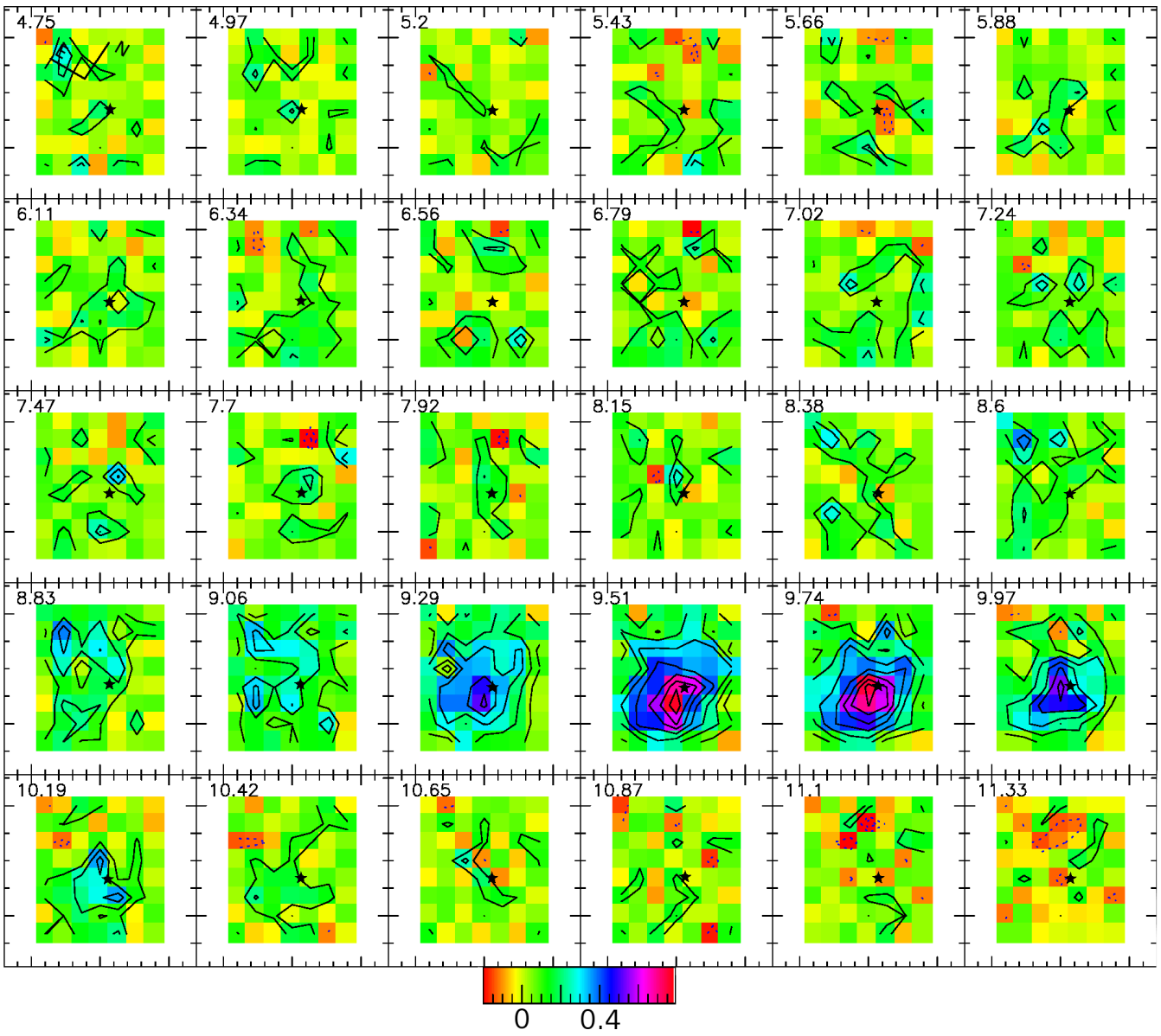


**Fig. B.5.** As Fig. B.1 for CS (2−1). The lowest contour level and increment are 0.1 K km s$^{-1}$.

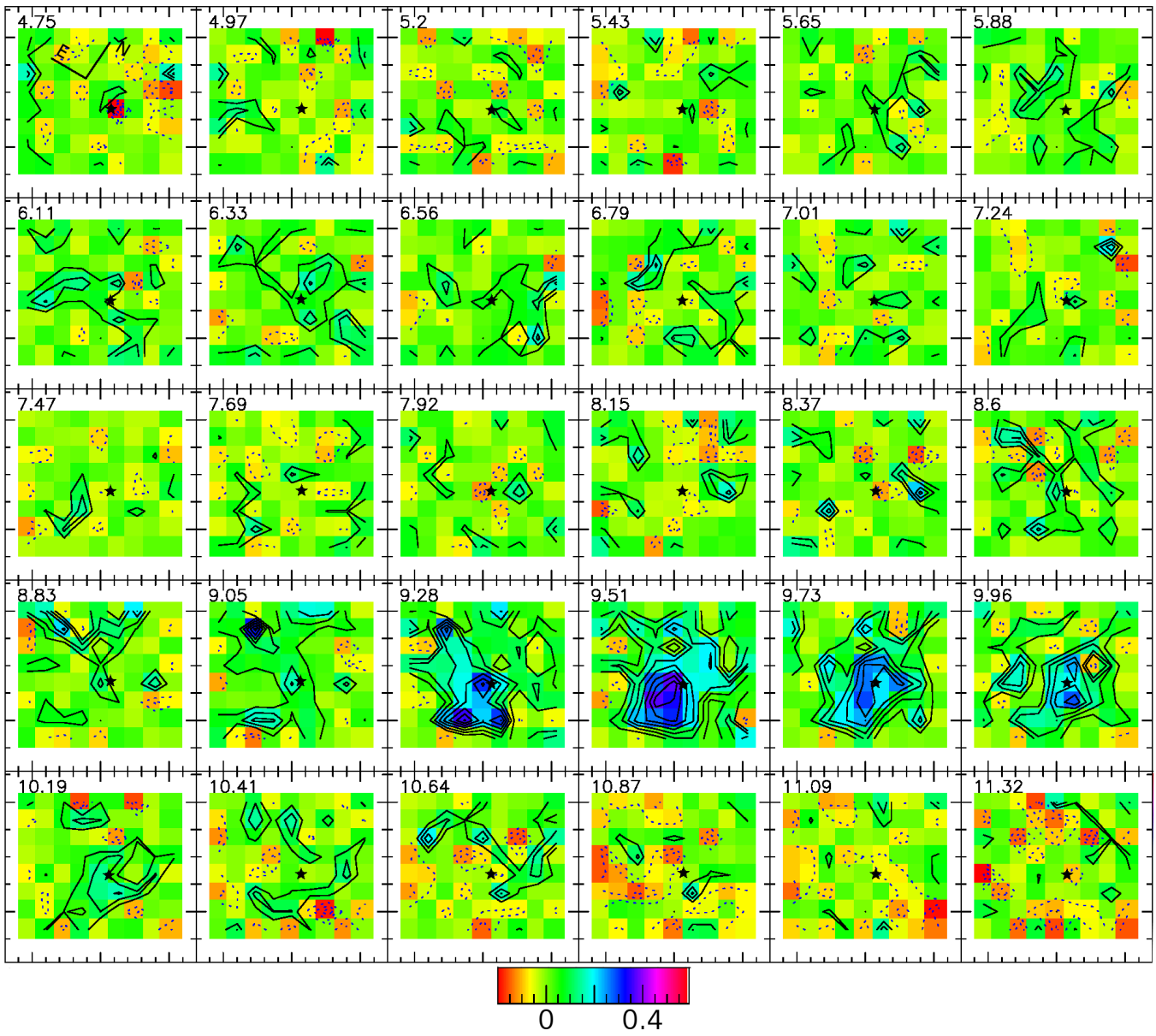


**Fig. B.6.** As Fig. B.1 for CS (3−2). The lowest contour level and increment are 0.05 K km s$^{-1}$.

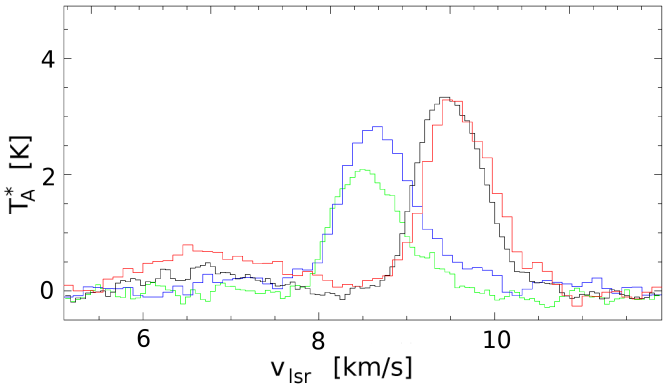


**Fig. B.7.** $^{13}$CO (1−0) and (2−1) spectra in off-positions 0″, 0″ (red and black) and 135″, 15″ (blue and green).

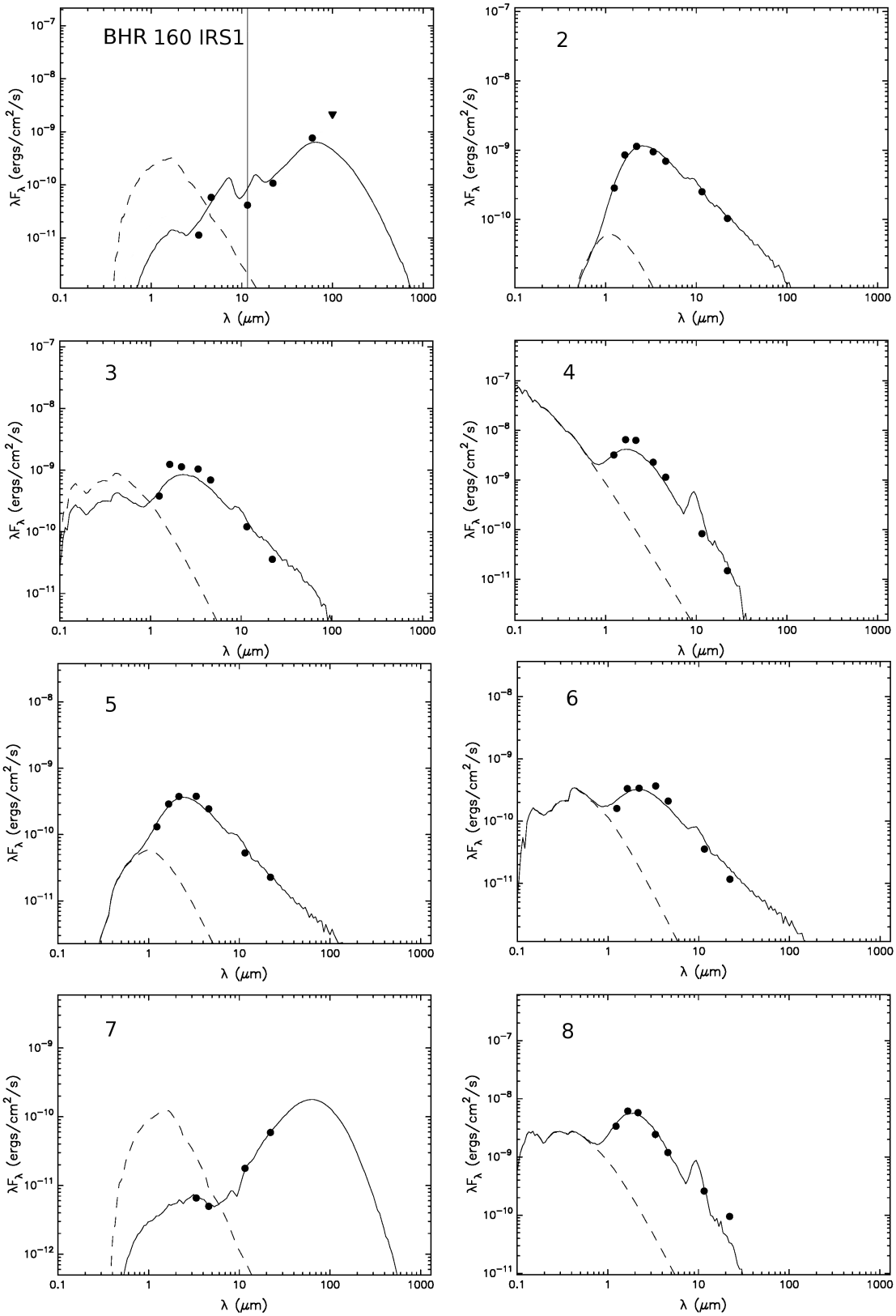


**Fig. B.8.** SED fits for the marked objects in Fig. 4. The filled circles are the observed fluxes and the triangle marks the BHR 160 IRS1 IRAS 100 $\mu$m flux upper limit. The dashed line indicates the SED of the unreddened stellar photosphere.